ELSEVIER

Journal of Structural Geology 30 (2008) 81–97

JOURNAL OF STRUCTURAL GEOLOGY

www.elsevier.com/locate/jsg

Stress and fracture prediction in inverted half-graben structures

Andreas Henk [a,*], Michal Nemčok [b]

[a] *Geologisches Institut, Universität Freiburg, Albertstrasse 23b, D-79104 Freiburg, Germany*
[b] *Energy & Geoscience Institute, University of Utah, 423 Wakara Way, Suite 300, Salt Lake City, UT 84108, USA*

Received 27 February 2007; received in revised form 12 September 2007; accepted 12 October 2007
Available online 17 November 2007

Abstract

Two-dimensional finite element models are used to study the temporal evolution and spatial distribution of stress and strain during half-graben inversion. Modeling is based on forward balanced cross-sections and involves various parameter studies to assess the impact of different syn- and post-rift lithologies as well as scenarios with syn-tectonic deposition or erosion, respectively. In total, 48 different scenarios were analyzed. Modeling results are presented as contour maps of total displacement, brittle plastic strain, mean stress and differential stress as well as vector diagrams showing the orientation of the principal stresses. This information can be combined to predict fracture types and fracture orientations and provide fracture intensity maps throughout the evolving inversion structure. Modeling results demonstrate quantitatively how stress and strain in inverted half-grabens critically depend on the rheology of the syn- and post-rift sediments and their mechanical interaction as well as the stress transfer through the hanging wall. Four end-member scenarios can be identified on the basis of distinct fault reactivation tendencies, deformation styles and fracture patterns. Model predictions are compared to natural examples of inverted half-graben structures using seismic as well as outcrop data. Thus, the geomechanical models can provide templates for a reservoir- (kilometer-) scale prediction of tectonic stresses and fractures for a common type of inversion structure.

Keywords: Inversion; Half-graben; Stress prediction; Fracture prediction; Numerical modeling

1. Introduction

Basin inversion describes the evolution of an extensional basin that has subsequently undergone compression leading to reactivation of pre-existing faults and uplift of the basin fill (Gibbs, 1987; Koopman et al., 1987; Cooper et al., 1989; Coward, 1994, and references therein). The response of sedimentary basins to changing stress fields has attracted a lot of attention in the past two decades, particularly because inversion structures form important hydrocarbon traps (e.g., Bally, 1983; Selley and Stoneley, 1987; Roberts, 1989; Uliana et al., 1995). Valuable contributions improving our understanding of the mechanisms controlling basin inversion and the related structural styles were made by analogue and numerical modeling (e.g., Buchanan and McClay, 1991; Nalpas et al., 1995; Brun and Nalpas, 1996; Sassi and Faure, 1996; Ferguson and McClay, 2000; Beekman et al., 2000). The modeling was done at various scales. For example, McClay (1995) used scaled sand-box models to reproduce the structural architecture observed in inverted sedimentary basins, whereas Buiter and Pfiffner (2003) applied a numerical approach to examine the inversion of a half-graben system on an upper crustal scale.

From such analogue and numerical studies, fault geometry, fault reactivation tendency, lithology and geometry of the basin fill, syn-inversional sedimentation and erosion and the amount of shortening have been identified as the most important factors controlling basin inversion (e.g., McClay, 1995, and references therein). For example, the lower, flatter portions of listric fault planes can be easily reactivated as thrusts, whereas reactivation of the higher, steeper portions as reverse faults is mechanically more difficult (e.g., Panien et al., 2005). For large amounts of horizontal shortening, inversion can be associated with strong uplift and intense deformation of the

* Corresponding author. Tel.: +49 0761 2036471; fax: +49 0761 2036496.
E-mail address: henk@uni-freiburg.de (A. Henk).

0191-8141/$ - see front matter © 2007 Elsevier Ltd. All rights reserved.
doi:10.1016/j.jsg.2007.10.006

basin fill (Letouzey et al., 1990). Inversion frequently results in propagation of the main fault into the post-rift and syn-inversion section and development of shortcut faults in the footwall edge (Fig. 1). At large amounts of shortening, these shortcut faults may take the form of low-angle thrust planes and result in the incorporation of exotic basement slices into the inversion structure. In cases where extension has formed crestal collapse grabens and antithetic faults, inversion compresses these features producing pop-up structures bounded by reverse and thrust faults. If inversion is accompanied by deposition, growth anticlines can form over the reactivated faults.

Here we present the results of a systematic numerical study focusing on a detailed analysis of the temporal evolution and spatial distribution of stresses and strains during basin inversion. Our approach is to apply finite element models to various stages of half-graben inversion which were generated from step-wise geometric balancing. Modeling results provide displacement, brittle plastic strain, differential and mean stress distribution patterns as well as orientations of principal stresses, which are combined to determine the fracture patterns which were active during the various inversion stages. Models are designed to provide hydrocarbon field-scale (kilometer-scale) geometry of the inverted basin fill. The half-graben geometry was selected because it is a common structural element that undergoes subsequent compression in numerous natural cases. Examples of such inverted half-grabens come from the North Sea (e.g., Badley et al., 1989; Nalpas et al., 1995), the north Pyrenees (Hayward and Graham, 1989), the Walls Basin, British Isles (Coward et al., 1989), Salta province in northern Argentina (Lowell, 1995), the Gippsland Basin, Australia (Davis, 1983), southern Altiplano, Bolivia (Lowell, 1995), and Dnepr-Donetsk, Ukraine (Ulmishek et al., 1994).

2. Modeling approach

Finite element (FE) techniques were used to gain quantitative insights into the stress and strain distribution during basin inversion. This method was chosen because it allows robust numerical simulations even for heterogeneous structures with complex geometries and non-linear material behavior. Model geometries describing different stages of half-graben inversion were made by forward balancing from initial to most mature inversion stages using the 2D Move® (Midland Valley Exploration Ltd., Glasgow, UK) software. Rock mechanic data were added after transferring the various balancing stages into the FE program ANSYS® (Ansys Inc., Houston, TX), which was then used to calculate various stress and strain parameters during step-wise basin inversion. Several parameter studies based on the same model geometries were carried out to study the effects of basin lithology and syn-tectonic deposition/erosion on the modeling results.

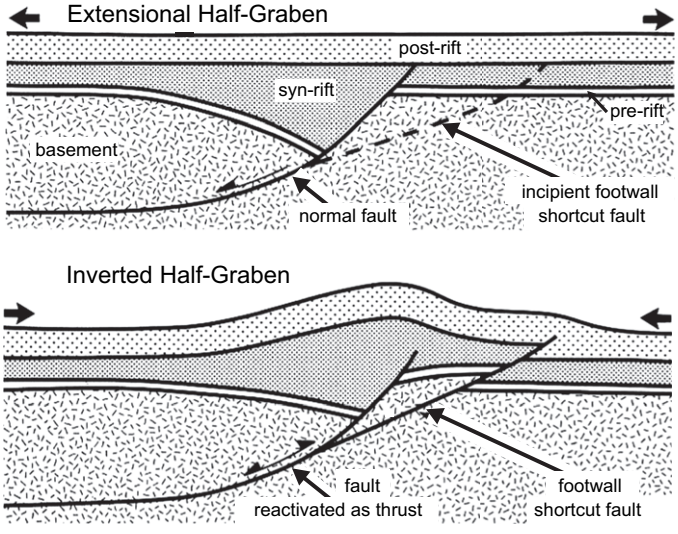

Fig. 1. Typical structures associated with inverted half-graben basins (modified after Cooper et al., 1989).

2.1. Model geometry

Models describe cross-sections through four stages of an evolving inverted half-graben (Fig. 2). Due to the two-dimensional character of the models, the effect of oblique convergence and transpression, respectively, cannot be considered. The basic structural scenario is represented by a half-graben bounded by a listric normal fault, which is sequentially reactivated as thrust and reverse fault in its flat and steep portions, respectively. The initial depth-to-detachment is 4.2 km and the maximum dip angle of the fault plane reaches 60 ° in its uppermost part. The listric normal fault is defined as relatively weak, resulting in its preferential reactivation when its failure conditions are met during inversion. The initial model domain covers an area of 15.75 km width and 5.7 km thickness (Fig. 2, top). The three other cross-sections represent the inverted half-graben structure after 365 m, 720 m and 975 m of horizontal convergence. This is equivalent to 4.4%, 8.6% and 11.7% shortening with respect to the initial width of the half-graben. The lithological layering implemented in the initial model geometry comprises a 700 m thick post-rift sequence of either shale or sandstone. It is underlain by a syn-rift section of either limestone or sandstone or shale lithology, which thickens to its maximum thickness of 2 km next to the graben-bounding normal fault. It rests on a 200 m thick pre-rift layer of sandstone, which in turn lies on crystalline basement represented by granite. All modeled scenarios experienced either deposition keeping up with the growing structure or 50% erosion during simulated shortening, in order to study basin inversion in marine and continental setting, respectively.

2.2. Numerical model

ANSYS® uses a Lagrangian formulation to simulate two-dimensional, plane strain deformation using four-node isotropic elements to represent the individual lithological layers. Their mechanical behavior in the elastic domain is described by the generalized Hooke's law, relating strains ε to stresses σ via Young's modulus E and Poisson's ratio ν (e.g., Turcotte

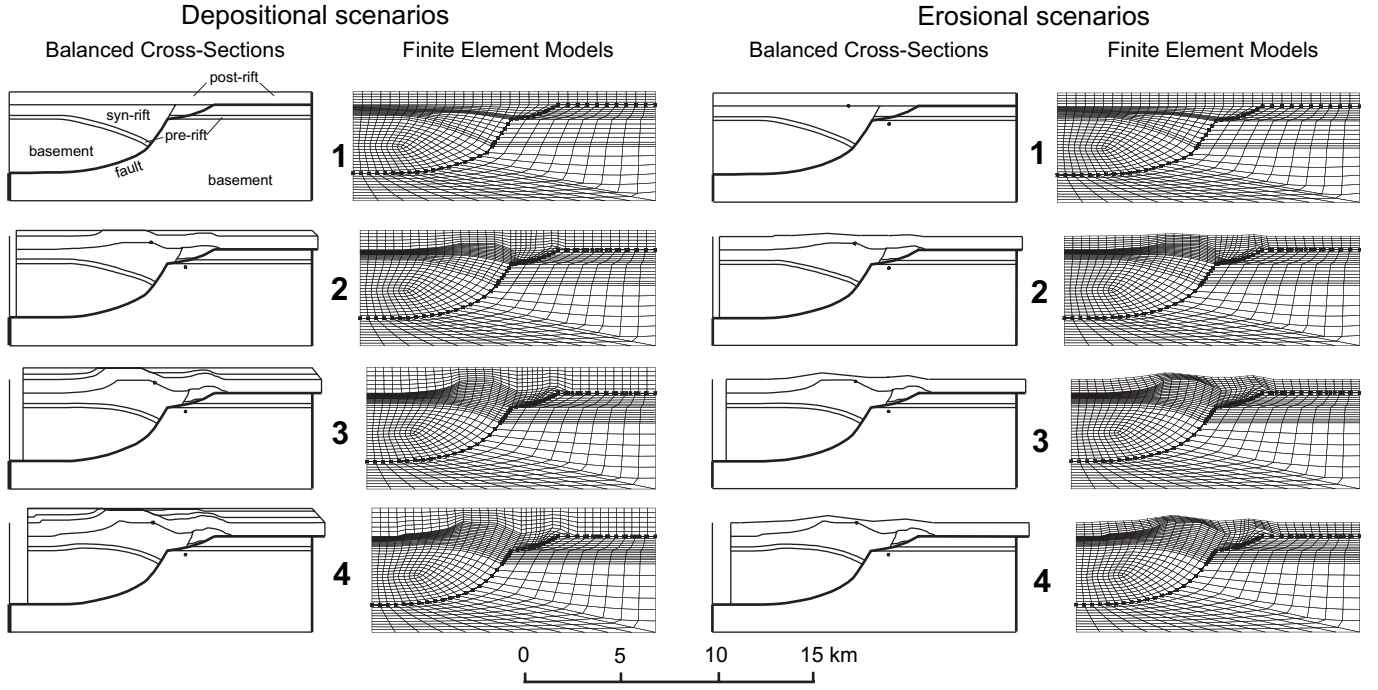

Fig. 2. Step-wise forward balanced cross-sections and corresponding finite element models of the depositional (left) and erosional (right) scenarios. The top row shows the initial model geometry prior to inversion (stage 1), while the remaining three rows represent the inverted half-graben structure after 365 m, 720 m and 975 m of horizontal convergence (stages 2, 3 and 4). This is equivalent to 4.4%, 8.6% and 11.7% shortening with respect to the initial width of the half-graben.

and Schubert, 2002) under plane strain conditions ($\varepsilon_2 = 0$) according to:

$$\varepsilon_1 = \frac{(1+\upsilon)}{E}[\sigma_1(1-\upsilon) - \upsilon\sigma_3] \quad (1)$$

$$\varepsilon_3 = \frac{(1+\upsilon)}{E}[\sigma_3(1-\upsilon) - \upsilon\sigma_1] \quad (2)$$

Brittle failure is governed by the Coulomb criterion (e.g., Jaeger and Cook, 1979) according to

$$\tau_{crit} = c + \mu\sigma_n \quad (3)$$

where τ_{crit} is the critical shear stress, c is the cohesion, μ is the coefficient of internal friction and σ_n is the stress normal to shear fracture. The volume increase due to grain rearrangement during the initial stages of fracturing is controlled via the angle of dilatancy ψ (Mandl, 1988) according to:

$$\psi = \arcsin\left(-\frac{d\varepsilon_1^{pl} + d\varepsilon_3^{pl}}{d\varepsilon_1^{pl} - d\varepsilon_3^{pl}}\right) \quad (4)$$

where $d\varepsilon_1^{pl}$ and $d\varepsilon_3^{pl}$ are the major and minor principal brittle plastic strain increments. It needs to be emphasized that the models presented here do not contain viscous materials. The finite element modeling approach, however, allows incorporation of other types of material behavior such as, for example, temperature-dependent creep laws for evaporites.

Each of the finite-element models is cut by planes of weakness, i.e. the pre-existing faults inherited from the extensional stage. These planes are described by so-called contact elements. This approach allows for large movements between the different, individually meshed parts of the model, but does not describe fault propagation itself. Contact elements are defined at opposing sides of the pre-assigned faults. Stiffness values similar to the Young's moduli of the rocks in contact are used to enforce compatibility between adjacent fault surfaces. These contact elements are also capable of describing frictional sliding.

Depending on the development stage of the growing inversion structure, up to 2100 planar elements and 900 contact elements are used to represent the model geometry. The physical

Table 1
Physical rock properties used in the finite-element models

Lithology	Young's modulus (GPa)	Poisson's ratio	Cohesion (MPa)	Coefficient of internal friction	Angle of dilatancy (degrees)	Density (kg m^{-3})
Granite	70.60	0.18	55.1	1.23	17.0	2640
Limestone	77.40	0.26	26.8	0.50	8.8	2720
Sandstone	18.30	0.38	27.2	0.53	9.3	2180
Shale	5.52	0.25	0.7	0.38	7.0	2470

Values are taken from Clark (1966), Lama and Vutukuri (1978), Cloetingh et al. (1995), Beekman et al. (2000) and van Wees et al. (2003).

Table 2
Overview of the different model scenarios and the coding used

Surface process during inversion	Lithology of pre-rift basin fill	Lithology of syn-rift basin fill	Lithology of post-rift basin fill	Model code
syn-Tectonic sedimentation	Sandstone	Limestone	Sandstone	S-ss-li-ss
			Shale	S-ss-li-sh
		Sandstone	Sandstone	S-ss-ss-ss
			Shale	S-ss-ss-sh
		Shale	Sandstone	S-ss-sh-ss
			Shale	S-ss-sh-sh
syn-Tectonic erosion	Sandstone	Limestone	Sandstone	E-ss-li-ss
			Shale	E-ss-li-sh
		Sandstone	Sandstone	E-ss-ss-ss
			Shale	E-ss-ss-sh
		Shale	Sandstone	E-ss-sh-ss
			Shale	E-ss-sh-sh

For each of the 12 scenarios, four geometrical restoration stages (see Fig. 2) have been modeled, and, hence, 48 models were analyzed in total.

properties of the various lithologies assigned to the finite element models are summarized in Table 1. The lithologies selected for the basin fill, i.e. shale, sandstone and limestone, represent the range from mechanically weak to mechanically strong rock rheologies typically encountered in nature. Various parameter studies with different combinations of syn- and post-rift lithologies as well as depositional or erosional scenarios were carried out. A complete overview of all model runs is given in Table 2. In all scenarios, a friction coefficient of 0.4 has been assigned to the fault zone elements. This is based on the assumption that faults in lithologies like limestone, sandstone and granitic basement tend to be much weaker than the corresponding host rocks, as it is observed in hydrocarbon reservoirs worldwide (e.g., Townend and Zoback, 2000). Likewise, fault propagation of the footwall edge short-cut fault and frontal detachment fault may be preceded by micro-fracturing (e.g., Scholz, 1968). This also reduces the friction coefficient of the host rock, which would be 0.38 and 0.53 for shale and sandstone, respectively (e.g., Nemčok et al., 2005, and references therein). Thus, as long as no specific fault friction coefficients are known, a value of 0.4 is considered a reasonable approximation for fault strength in the basement and sedimentary cover. The modeling approach, however, is open for different friction coefficients along the various fault segments.

Boundary conditions for the inverted half-graben models (Fig. 3) include a base fixed in vertical direction. The lower parts of the left and right side walls are constrained with respect to horizontal movements. The top of the model, i.e. the earth's surface, forms a free surface. The entire model is subject to gravity forces. Stresses in the finite element models are built up by block motions, i.e. movement of the hanging wall relative to the footwall. Displacement constraints are applied to the nodes on the left side of the hanging wall to simulate compression. A lithostatic pressure boundary condition is applied to the upper part of the right side of the model to represent propagation of the inversion structure towards the "free" foreland. Models are run until excessive mesh distortion and/or mesh penetration at the contact elements cause an instable numerical solution. This typically occurs after 80–100 m of total convergence.

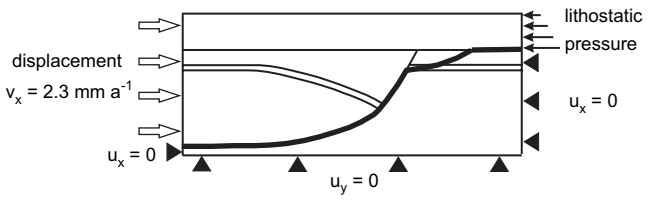

Fig. 3. Boundary conditions of numerical model.

3. Results

Due to the large number of possible combinations in syn- and post-rift lithologies placed into erosional or depositional settings for each of the four inversion stages (see Table 2), only a selection of the modeling results can be shown here for spatial reasons. We focus on end-member scenarios and discuss general trends in displacement, strain, stress and fracture distributions. Modeling results are presented as maps of total displacement (vector sum of horizontal and vertical movements), brittle plastic strain, mean stress and differential stress. As only an approximate description of the real sediment rheology is used, we do not attempt to predict absolute values but concentrate on the relative patterns of stress and deformation in relation to different inversion stages, basin lithologies and syn-inversion deposition/erosion. For selected models, this information is combined with principal stress orientations to illustrate the potential of the modeling approach for predicting fracture types, fracture orientations and fracture intensities.

3.1. Deformation

Deformation of the evolving inversion structures can be analyzed by a combined interpretation of total displacement and brittle plastic strain patterns. Different amounts of displacement across the faults point towards movement along the pre-defined faults, whereas high-strain zones indicate where future faults will develop.

Scenarios containing strong syn- and post-rift sedimentary sections form the first end-member in the spectrum of modeled deformation patterns. The inversional structure formed by the

limestone syn-rift and sandstone post-rift sections undergoes a reactivation/formation of the most complex fault system, which includes the reactivated listric normal fault, the footwall edge shortcut fault and the frontal detachment fault (Fig. 4a). Plastic deformation leading to brittle failure is restricted to the syn-rift basin fill. The strain pattern points towards formation of a back-thrust along which the wedge-shaped, thickest part of the half-graben is uplifted. A similar distribution of fault movement and strain can be observed in all four inversion stages for both erosional and depositional settings of this scenario.

Fault activity and strain distribution change dramatically if a mechanically strong syn-rift section, e.g. limestone, coexists with a mechanically weak post-rift lithology, e.g. shale. In this case, a frontal detachment fault is not formed and a high-strain

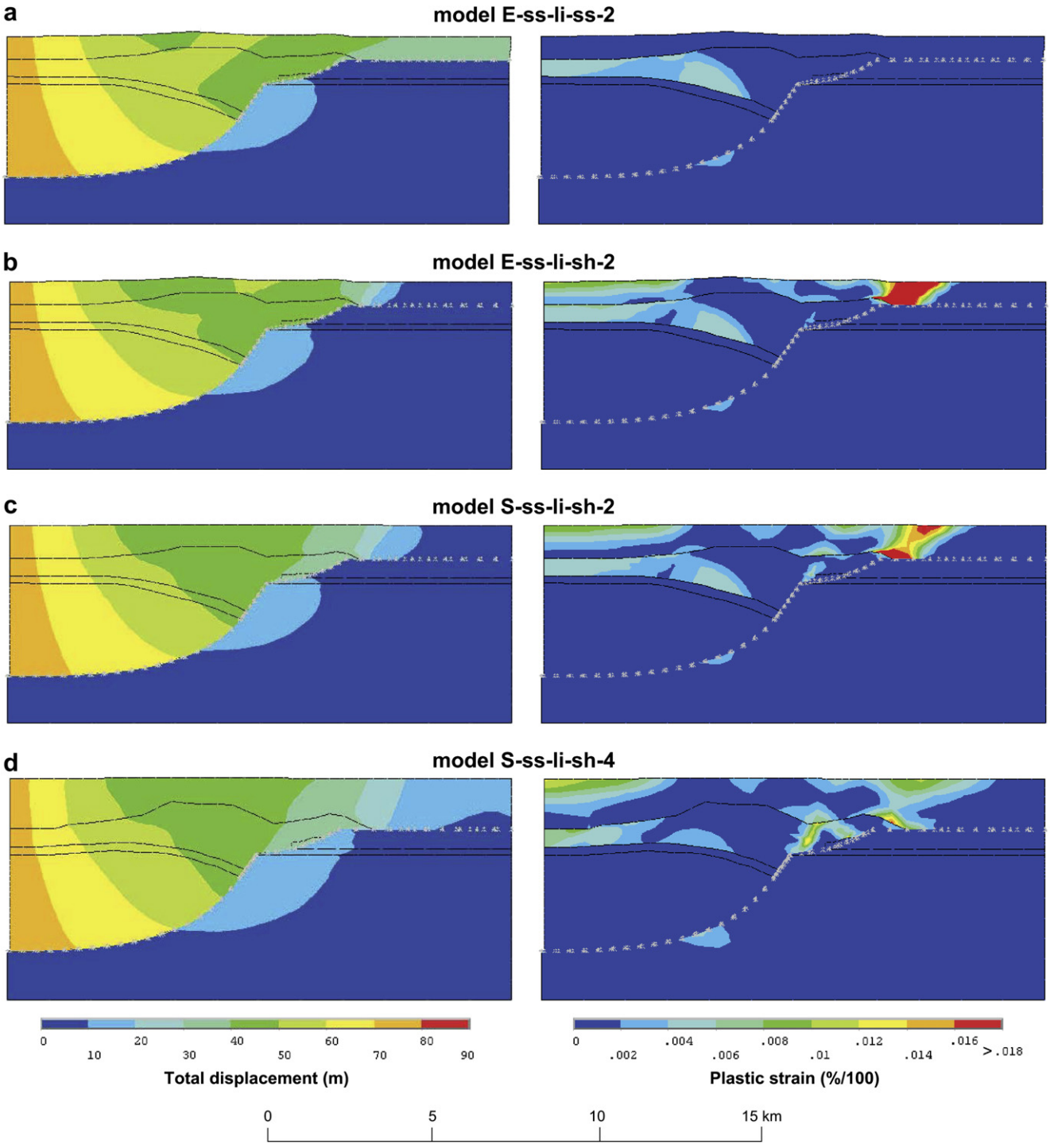

Fig. 4. Total displacement (left) and brittle plastic strain (right) distribution for selected model scenarios. Model coding indicates erosion (E) or deposition (S), pre-, syn- and post-rift lithology (ss, sandstone; lm, limestone; sh, shale) as well as the inversion stage (see also Table 2 and Fig. 2). See Section 3.1 for detailed description.

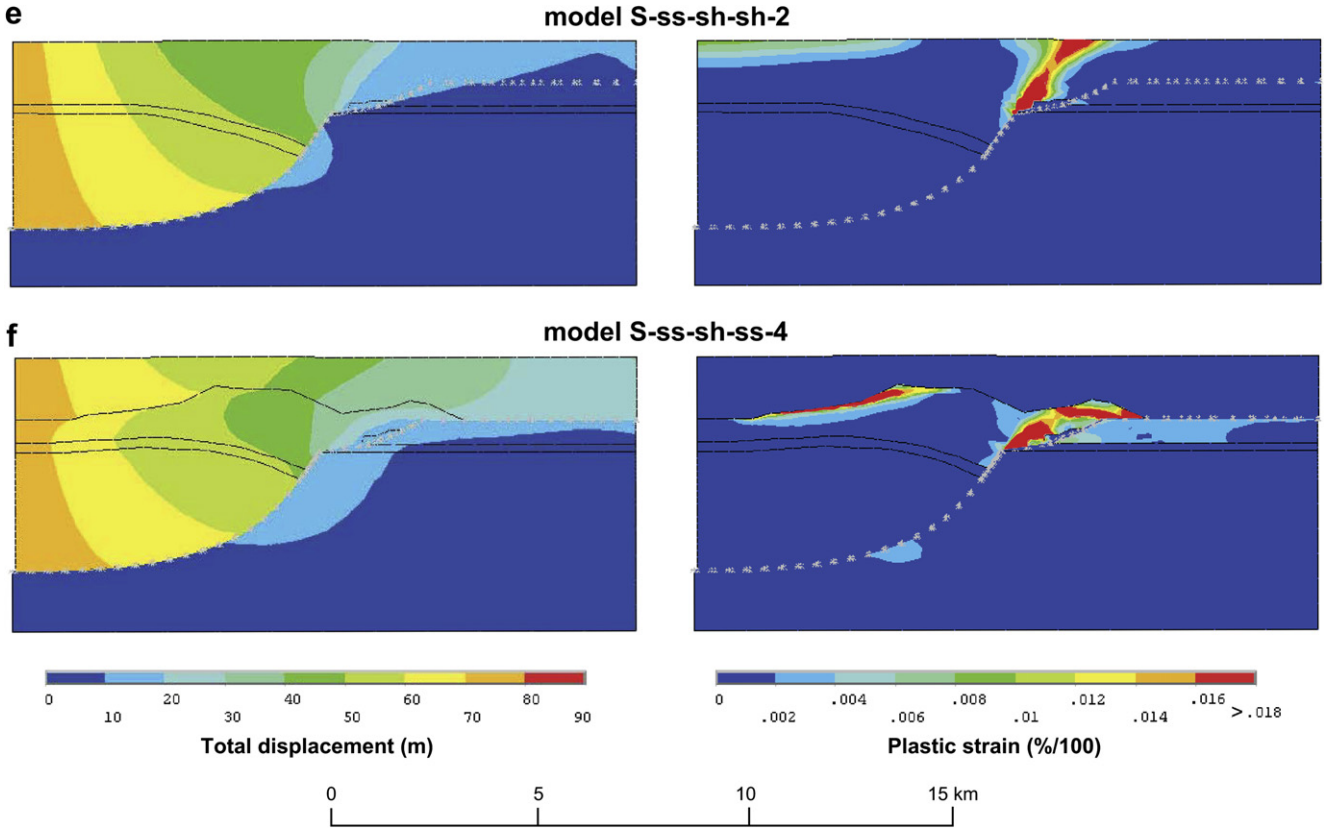

Fig. 4 (*continued*).

zone develops in the post-rift sediments in continuation of the footwall edge shortcut fault (Fig. 4b). Each movement of the footwall edge shortcut fault is propagated through the mechanically weak post-rift sediments to the surface without transfer to the frontal detachment fault. The strain pattern in the syn-rift sediments is not significantly different from the scenario shown in Fig. 4a.

In case of mechanically weak post-rift sediments, fault activity and strain distribution also depend on the inversion stage and presence of syn-inversional deposition. With increasing thickness of the post-rift sedimentary section and with growth of the inversion structure in depositional scenarios, respectively, the intense deformation zone along the upward continuation of the footwall edge shortcut fault moves to the location along the upward continuation of the reactivated normal fault (compare Fig. 4c and 4d). Thicker post-rift sediments enhance movement along the frontal detachment fault. In contrast, erosion during inversion focuses deformation along the upward continuation of the footwall edge shortcut fault without any foreland-directed movement along the frontal detachment fault.

If both syn- and post-rift sections consist of mechanically weak sediments, i.e. shale, movement of the hanging wall is taken up primarily by the main basin-bounding fault (Fig. 4e). Movements along the footwall edge shortcut fault and frontal detachment fault play only a very minor role. The model results show a very pronounced strain zone in up-dip continuation of the steep section of the main listric fault suggesting fault propagation through the sediments towards the surface. The syn-rift section outside this zone remains largely undeformed.

The fourth type of inverted half-graben deformation is controlled by a mechanically weak syn-rift basin fill overlain by strong post-rift sediments, i.e. shale covered by sandstone. In this case, deformation is restricted entirely to the syn-rift sediments (Fig. 4f), particularly to the wedge above the footwall edge shortcut fault. Like in the previous scenario (see Fig. 4e), a continuation of the main fault has developed in the syn-rift sediments but does not propagate into the post-rift sandstone section. All three pre-defined fault segments are active resulting in a foreland-directed movement along the frontal detachment fault.

With respect to footwall deformation, some straining usually occurs near the largest curvature of the listric fault plane, particularly for models with strong syn- and/or post-rift lithologies (limestone, sandstone). Similarly, the largest displacements are found in cases of strong half-graben fills, whereas for weak sediments there is hardly any footwall dislocation.

3.2. Mean stress

Mean stress, i.e. the algebraic mean of the principal stresses, provides information on deformation control and the dynamic constraint to fluid flow. Mean stress shows a more uniform distribution than deformation. The highest mean stresses always occur in the basement of the hanging wall block, particularly in the vicinity of the listric fault. High stresses can be also accumulated in the syn-rift sediments if mechanically strong lithologies such as limestone are involved. For example, the half-graben model with strong syn- and post-rift sections represented by limestone

and sandstone, respectively, develops high mean stresses in the deepest part of the syn-rift section next to the main fault where the hanging wall is pushed against the footwall buttress (Fig. 5a). The lowest mean stresses with even slightly negative values are located in the inversional anticline affecting not only the post-rift, but also part of the syn-rift section. This observation holds for all inversional stages of the erosional scenario. The associated depositional scenario shows the higher mean stresses in the basement as well as in the pre- and syn-rift sediments (Fig. 5b). If erosion is considered, the area with negative mean stresses (Fig. 5a) almost vanishes (Fig. 5b). Similar mean stress patterns and differences between syn-inversional erosion and sedimentation are also observed for scenarios which involve sandstones as syn- and post-rift lithologies.

If a mechanically strong syn-rift fill is capped by weak post-rift sediments, an isolated negative mean stress anomaly develops in the crest of the inversional anticline of the erosional scenario (Fig. 5c). Unlike the case involving only mechanically strong layers (Fig. 5a), the negative mean stresses are confined to the uppermost syn-rift section (Fig. 5c). If sedimentation is added, mean stresses are higher, but the stress gradient between the deepest and highest parts of the syn-rift section remains similar (compare Fig. 5c and d). Similar mean stress patterns are typical for erosional and depositional scenarios in which syn-rift sandstone is covered by post-rift shale.

If syn-rift sediments consist of mechanically weak shale, higher mean stresses are confined to the basement and the pre-rift layer of the hanging wall block. In the syn-rift section higher mean stresses are observed only in a restricted area next to the footwall buttress.

3.3. Differential stress

The differential stress distributions for the various scenarios always show the largest differential stresses near the top of the basement in the hanging wall. All models indicate a systematic spatial shift of the corresponding differential stress maximum with progressive inversion. Initial inversion stages are characterized by the existence of the differential stress maxima located in the mechanically strong layer of the hanging wall, i.e. near the left side of the model and next to the footwall buttress (Fig. 6a). As inversion advances, the maximum next to the buttress gradually diminishes, while the maximum next to the left model boundary is further enhanced. If the model contains a mechanically strong syn-rift lithology, e.g. limestone, high differential stresses also develop in the basement of the footwall (Fig. 6c).

Maximum differential stresses in the syn-rift fill are associated with mechanically strong lithologies such as limestone and sandstone. High differential stresses typically occur along the base of the syn-rift section and above the footwall edge shortcut fault (Fig. 6a,b). If weak rheologies like shale represent the syn- and post-rift sections, they are characterized by low differential stresses (Fig. 6d). If erosional and depositional

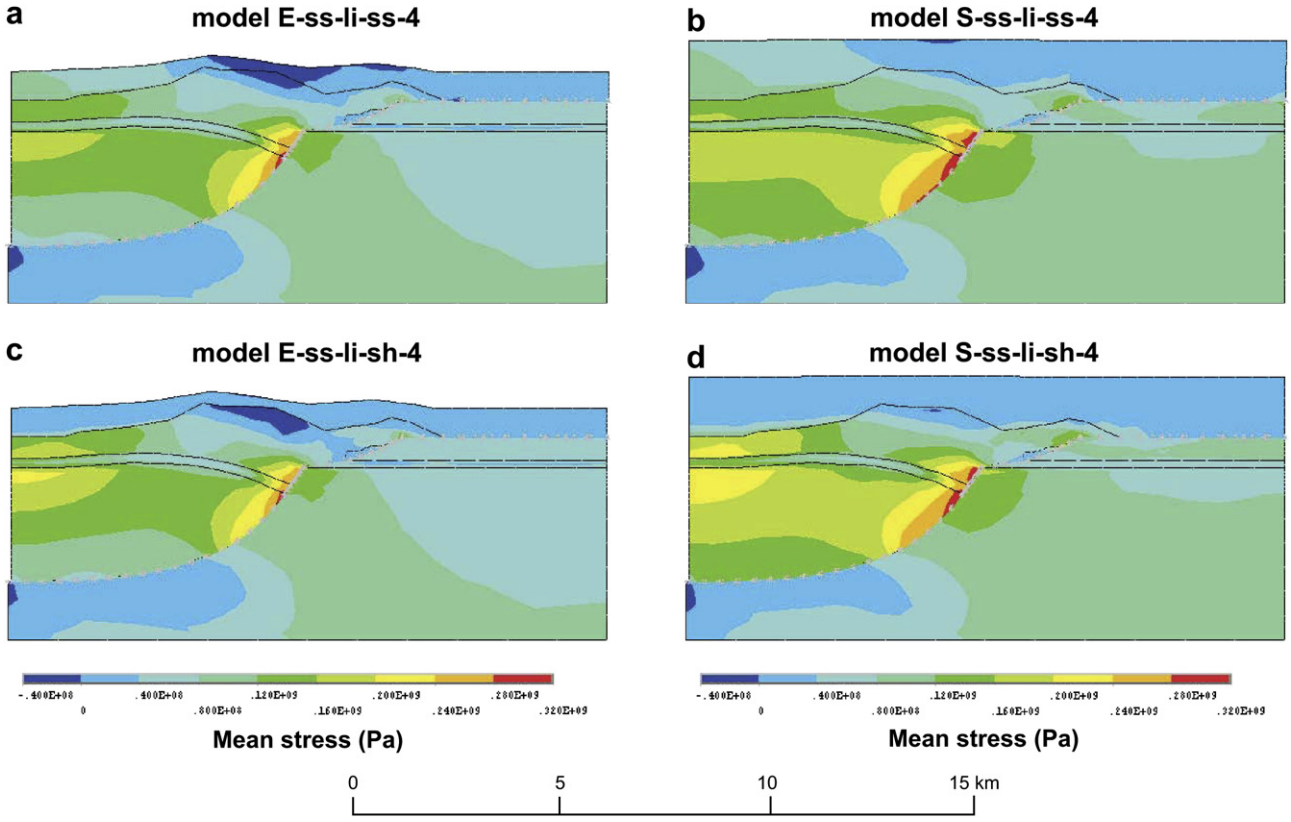

Fig. 5. Mean stress distribution for selected model scenarios. Model coding indicates erosion (E) or deposition (S), pre-, syn- and post-rift lithology (ss, sandstone; lm, limestone; sh, shale) as well as the inversion stage (see also Table 2 and Fig. 2). See Section 3.2 for detailed description.

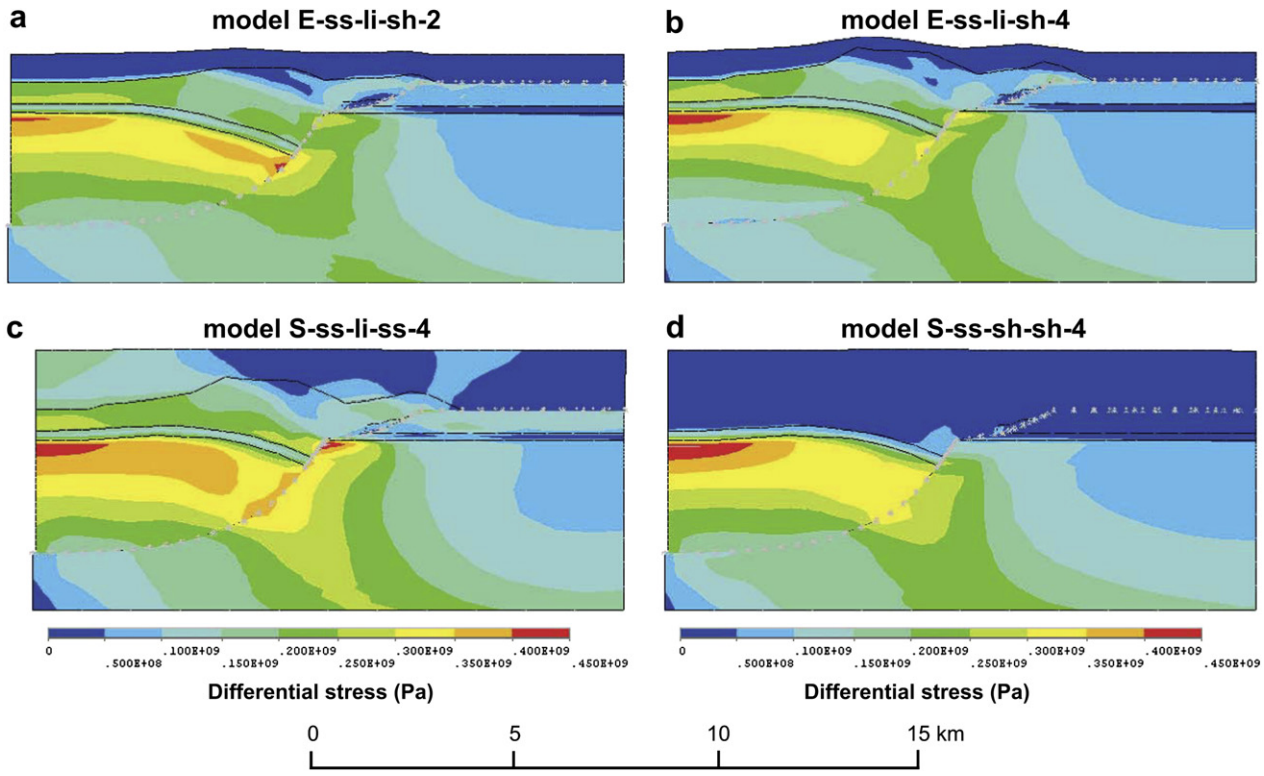

Fig. 6. Differential stress distribution for selected model scenarios. Model coding indicates erosion (E) or deposition (S), pre-, syn- and post-rift lithology (ss, sandstone; lm, limestone; sh, shale) as well as the inversion stage (see also Table 2 and Fig. 2). See Section 3.3 for detailed description.

variants of the same scenario are compared, the larger differential stresses are always present in the syn-inversional deposition case, while the respective stress pattern remains mostly unchanged.

3.4. Principal stresses and fractures

As the geomechanical models provide the full stress tensor for all nodal points, it is also possible to infer the local orientations and magnitudes of the principal stresses. This information can be used in combination with brittle plastic strain and differential stress distributions to calculate failure mechanisms and controlling stresses, and to predict fracture orientations and relative fracture intensities. According to Sibson (1996), the following stress conditions can be used to define the type of fracture:

extension fracture:

$$(\sigma_1 - \sigma_3) < 4T \tag{5}$$

extensional shear fracture/hybrid fracture (Griffith criterion):

$$4T < (\sigma_1 - \sigma_3) < 6T \tag{6}$$

shear fracture (Coulomb criterion):

$$(\sigma_1 - \sigma_3) > 6T \tag{7}$$

where T is tensile rock strength, taken as $T = 0.5C$, i.e. as half of the cohesive strength of the various rock types (Table 1).

Fig. 7a illustrates such modeling results for an erosional scenario with pre-rift sandstone, syn-rift limestone and post-rift shale sections in the initial growth stage. It focuses on the basin fill and stress and fracture distributions are shown only for such areas where stresses have exceeded the brittle strength of the sedimentary rocks and brittle plastic straining has occurred.

The syn-rift limestone section of this scenario is mechanically much stronger than the post-rift shale section. The model is characterized by separate fracture systems in the syn-rift and post-rift sections (Fig. 7a). The angles, Φ, between conjugate sets of shear fractures in these two sections differ from each other, being controlled by the different angles of internal friction, φ, according to

$$\Phi = \pm 90^{\circ} - \varphi \tag{8}$$

The post-rift section undergoes shear fracturing at low differential and mean stress levels almost everywhere. Sub-horizontally oriented negative minimum principal stresses σ_3 occur above the crest of the main anticline and close to surface. This results in development of the sub-vertical extensional shear fractures, which have strikes parallel to the fold axis.

The syn-rift section shows a significant deflection of stress trajectories, which reaches up to 20 ° in the main anticline and the smaller anticline above the footwall edge shortcut fault

(Fig. 7a). Shear fractures in the syn-rift section are developed almost everywhere in areas of brittle plastic strain. The only exceptions are the uppermost frontal limb of the main anticline and two small areas around the footwall edge shortcut fault, which are deformed by extensional shear fractures and extension fractures. These three areas do not reach high enough differential stresses for shear fracturing but develop negative σ_3 stresses. The σ_3 stress has a dip of 0–20 ° in the upper portions of both anticlines and ~90 ° in the basal portion of the core of the anticline located above the footwall edge shortcut fault.

Shear fractures in the entire model are represented by thrusts with exception of the three regions where the intermediate and minimum principal stresses have exchanged their positions. In these regions, σ_3 is perpendicular to the cross section, whereas normally σ_3 lies in the section. Mentioned special stress conditions occur:

(1) in the post-rift section on the pro-side of the main anticline,
(2) close to surface on the retro-side of the main anticline, and
(3) in the crest of the syn-rift anticline above the footwall edge shortcut fault.

They control formation of strike-slip and oblique-slip fractures.

The model contains two areas without brittle plastic straining. The first area extends from the tip of the main normal fault to the crest of the syn-rift anticline (Fig. 7a). It comprises the strong syn-rift section, as the thickness of the mechanically strong syn-rift sediments has been further increased by folding with respect to adjacent areas. In addition, the amount of strain and shear fracturing decreases in direction from indenter to buttress, in accordance with stress transfer decrease in this direction. One more controlling factor is that the hanging wall in front of the strain-free area can move relatively easily along the footwall edge shortcut fault and, therefore, the buttressing in front of this area vanishes. The second strain-free area is located in the pre-rift section of the hanging wall above and parallel to the main normal fault. This may be caused again by the general decrease of stress transfer and associated shear fracturing with increasing distance from the indenter. The main fault is apparently weak enough to prevent buttressing, which is further minimized by the footwall edge shortcut fault that helps with moving the hanging wall towards the foreland.

Fig. 7b documents the stress and fracture development in a more advanced inversion stage of the model shown in Fig. 7a. The more advanced stage shows larger areas deformed by both extension and extensional shear fractures in the syn-rift section. They occupy substantial portions of the frontal limb of the main anticline and the crest of the smaller anticline above the footwall edge shortcut fault. Extension and extensional shear fractures that deform the post-rift section also document a slight expansion in the top portion of the main anticline. They also start to occur at the crest of the anticline above the footwall edge shortcut fault.

The three areas with an out-of-plane σ_3 controlling strike-slip and oblique-slip fractures identified in Fig. 7a are reduced to two in this model (Fig. 7b). The area on the left side of the main anticline has disappeared, while the area on the frontal limb has remained but became smaller. The third area in the crest of the syn-rift anticline above the footwall edge shortcut fault has expanded and moved upward into the post-rift section.

Fig. 7c illustrates an advanced inversional stage of the depositional scenario with pre-rift sandstone, syn-rift limestone and post-rift sandstone sections. With respect to the previous model (Fig. 7b), pre-rift and syn-rift lithologies have remained the same but the post-rift section is represented by sandstone, which due to the Coulomb failure criterion becomes even stronger with addition of syn-inversional sediments. Brittle plastic strain and fracture distributions document that a strong post-rift cover causes the stress release to locate almost exclusively in the syn-rift section. Similar to the previous models, an area with no brittle plastic straining extends between the original tip of the main normal fault and the crest of the main anticline. All areas affected by brittle plastic strain are deformed by shear fractures with the exception of the syn-rift anticlinal crest above the footwall edge shortcut fault. This area undergoes some extensional shear fracturing. The same area is also characterized by sub-horizontal and out-of-plane σ_3 orientation.

4. Discussion

The modeling results show that deformation styles, stress distributions and related fracture patterns in inversion structures vary among four different end-members. Potential limitations for the application of our numerical models to the real world, thus requiring further discussion, include:

(1) the prescribed fault geometries,
(2) the undisturbed state at the beginning of each model run,
(3) the frictional strength of the main boundary fault prescribed for the whole model run, and
(4) the rheologies for the various rift sections prescribed for the whole model run.

The modeled scenarios describing different stages of inversion contain faults, which are prescribed from forward-balanced sections (see Fig. 2); including:

(1) faults inherited from the extensional stage,
(2) a potential footwall edge short-cut fault, and
(3) a potential frontal detachment fault.

Subject to stress in dynamic models, the various prescribed faults can, but do not necessarily have to, be reactivated. Although it is frequently easier for the stresses building up during inversion to reactivate such already existing faults rather than to develop new ones, there are several model scenarios in which the prescribed faults are not reactivated. In such cases, the faults prescribed from geometric cross-section balancing, are mechanically not feasible and, thus, the ignored kinematic solution is not typical for the respective lithological

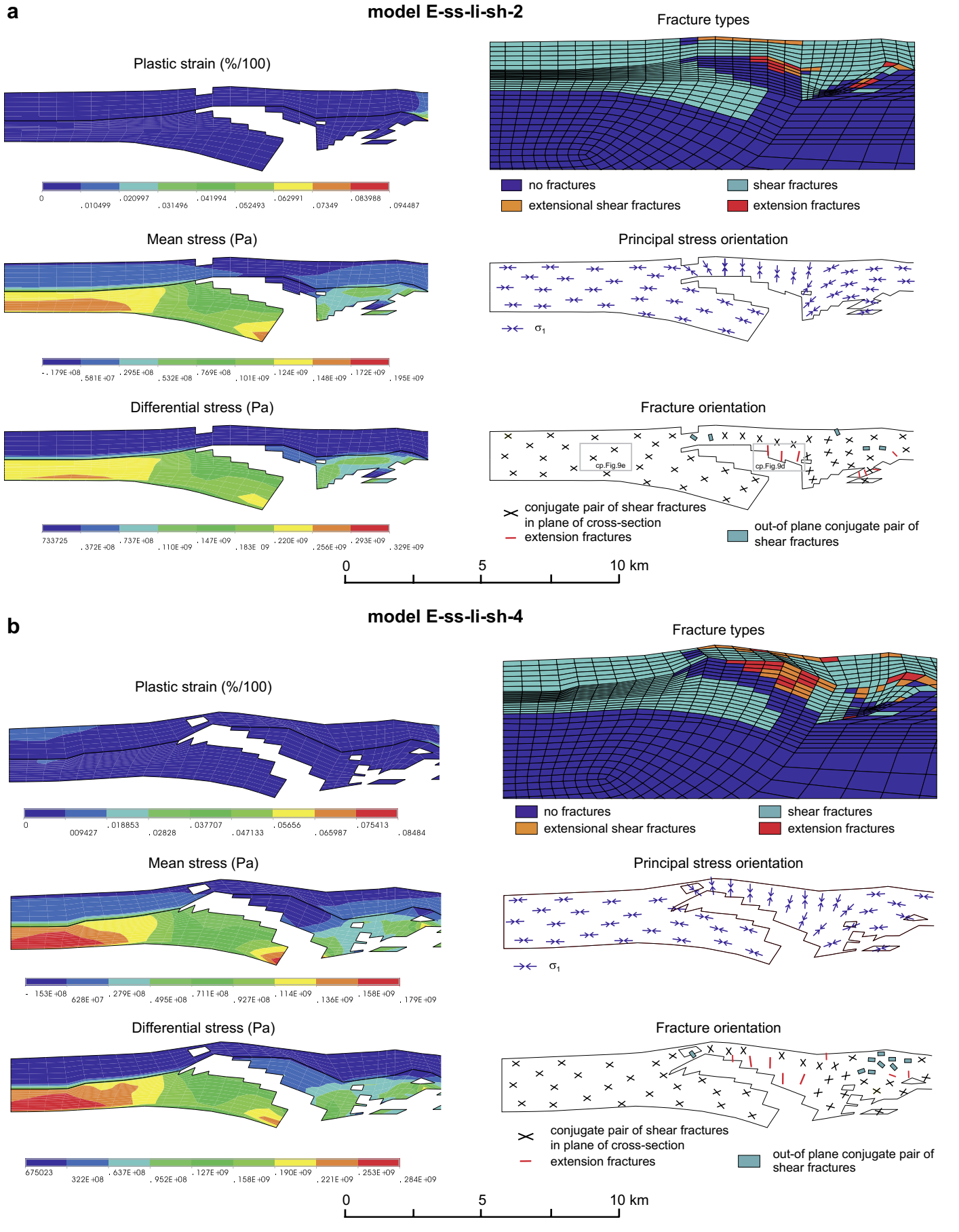
a
model E-ss-li-sh-2
Plastic strain (%/100)
0
.010499
.020997
.031496
.041994
.052493
.062991
.07349
.083988
.094487
Mean stress (Pa)
-.179E+08
.581E+07
.295E+08
.532E+08
.769E+08
.101E+09
.124E+09
.148E+09
.172E+09
.195E+09
Differential stress (Pa)
733725
.372E+08
.737E+08
.110E+09
.147E+09
.183E 09
.220E+09
.256E+09
.293E+09
.329E+09
Fracture types
no fractures
shear fractures
extensional shear fractures
extension fractures
Principal stress orientation
σ1
Fracture orientation
cp.Fig.9e
cp.Fig.9d
conjugate pair of shear fractures in plane of cross-section
extension fractures
out-of plane conjugate pair of shear fractures
0
5
10 km
b
model E-ss-li-sh-4
Plastic strain (%/100)
0
009427
.018853
.02828
.037707
.047133
.05656
.065987
.075413
.08484
Mean stress (Pa)
-.153E+08
628E+07
.279E+08
.495E+08
.711E+08
.927E+08
.114E+09
.136E+09
.158E+09
.179E+09
Differential stress (Pa)
675023
322E+08
.637E+08
.952E+08
.127E+09
.158E+09
.190E+09
.221E+09
.253E+09
.284E+09
Fracture types
no fractures
shear fractures
extensional shear fractures
extension fractures
Principal stress orientation
σ1
Fracture orientation
conjugate pair of shear fractures in plane of cross-section
extension fractures
out-of plane conjugate pair of shear fractures
0
5
10 km

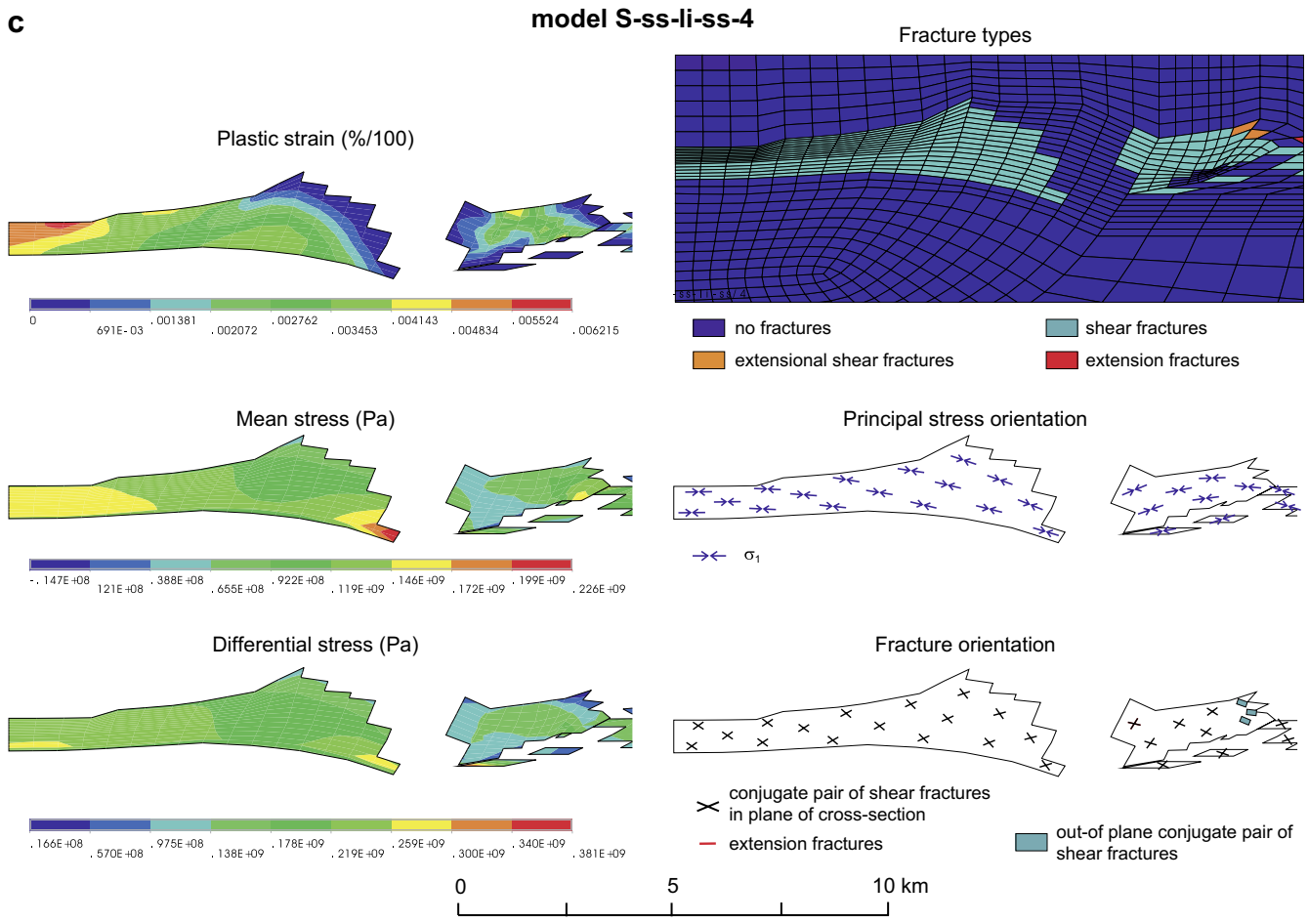

Fig. 7 (*continued*).

and erosional/depositional model. Therefore, dynamically modeled scenarios always indicate the deformational response of the specific lithological and erosional/depositional configuration, regardless of the pre-scribed "teasing" by geometric scenario. A choice to grow the modeled inversional structures in several stages is supported by case studies such as the interpretation of the high resolution 3D seismic images of several anticlines in the North Sea (Al-Musallam et al., 2002), where onlap patterns in the Upper Cretaceous syn-inversional strata allowed distinguishing of four deformation growth stages.

The models for each restoration stage start with intact rocks, i.e. deformation and fracturing, respectively, achieved during earlier inversion stages is not transferred to the next inversion step. This certainly is a simplification of natural processes and future simulations have to prescribe the fractures formed during previous stages to the next modeling step. However, material experiments by Kuhle et al. (2001) using a limestone syn-rift fill and a rigid 70 °-dipping normal fault indeed developed overprinting fracture sets in the model which would be in accordance with the assumption used for the numerical models presented here. This, perhaps, indicates that if we do not focus on specific fracture sets but rather on their general trends, we are allowed to discuss general interpretations, drawing from the same principle as the one chosen when modeling dynamic models using output of geometric balancing.

The comparison of the four end-member models indicates that fault reactivation and the deformational style of inversion critically depend on the rheology of the affected rock sections and how stresses are transmitted through the hanging wall and across the pre-existing faults. This corresponds with the outcomes of stress transfer studies (e.g., Geiser, 1974; Mandl, 1988; Koyi, 1995, 1997). Stress is transferred through the rocks by straining, which starts with initial elastic straining followed by plastic hardening and softening (e.g., Wojtal and Mitra, 1986; Mitra, 1987; Mandl, 1988) and depends on the layer rheology (Mitra, 1987; Mandl, 1988; Couples and Lewis, 1998), mechanic interaction of layers in the multilayer (e.g., Bott and Dean, 1973; Blay et al., 1977) and frictional properties of boundaries of multi-layered bodies through which the stress is transferred (e.g., Wiltschko and Eastman,

Fig. 7. Brittle plastic strain, mean stress, differential stress, fracture types, orientation of the maximum principal stress axis as well as fracture orientations for three model scenarios. For the last two parameters only selected modeling results are shown. Model coding indicates erosion (E) or deposition (S), pre-, syn- and post-rift lithology (ss, sandstone; lm, limestone; sh, shale) as well as the inversion stage (see also Table 2 and Fig. 2). See Section 3.4 for detailed description.

1983; Schedl and Wiltschko, 1987). Thus, only part of the shortening during inversion actually leads to differential fault movements while the rest is taken up by internal straining. This has already been indicated by analogue material experiments (Eisenstadt and Withjack, 1995; Yamada and McClay, 2003; Panien et al., 2005), which showed that model section balancing underestimates the shortening amount of experiments on inversional structures. A similar conclusion can be drawn from the numerical simulations presented here, which show substantial internal straining particularly in the hanging wall (Fig. 7) depending on the competence of the various rift sections.

With respect to the frictional strength and listric shape of the master fault, a sensitivity analysis has shown that a fault friction coefficient of 0.4 reveals a strong dependence of fault activity and strain distribution on the strength contrasts between the various parts of the modeled sedimentary section. A coefficient of 0.4, as discussed in the section on the numerical modeling approach, prevented stresses generated by hanging wall block motions (Figs. 3 and 4) from being funneled through the hanging wall above the reactivated fault and allowed for stresses to be transferred into the footwall (Figs. 5 and 6), as it is common in numerous natural examples where we see some footwall deformation (see also Fig. 9f).

The rheologies selected for the pre-, syn- and post-rift sections of the models are designed to approximate the mechanical behavior of natural multilayers, i.e. alternating sediment lithologies, which occur in extensional basins and later become affected by basin inversion. Studies of such multilayers involved in basement uplifts (Stearns and Weinberg, 1975; Friedman et al., 1976a,b, 1980; Logan et al., 1978; Weinberg, 1979; Couples et al., 1994; Couples and Lewis, 1998; Patton et al., 1998; Johnson and Johnson, 2002a,b) indicate that the deformational behavior of the multilayer is controlled by several factors such as the rheology and relative thicknesses of the individual layers, the degree of multilayer anisotropy and the degree of coupling between the multilayer and its basement. With respect to anisotropy the numerical models shown here represent a bulk description of natural multilayers with a relatively low anisotropy in each of the lithological units.

5. Comparison to field examples

5.1. Large-scale inversion structures

In order to assess the model predictions with respect to real inversion geometries, the calculated displacement and strain patterns of the four modeled end-members are compared to natural examples. Such inverted half-graben structures occur, for example, in intra-cratonic areas such as northwest Europe (e.g., Selley and Stoneley, 1987; Roberts, 1989; Fraser et al., 1990; De Jager et al., 1993), back-arc areas such as Sunda Arc or Pannonian basin system (Letouzey, 1990; Horváth and Cloetingh, 1996); and orogenic belts such as Andes or Carpathians (e.g., Uliana et al., 1995; Nemčok et al., 2006).

The first end-member with mechanically strong syn- and post-rift sedimentary sections as shown in Fig. 4a is characterized by a reactivated listric normal fault, and active footwall edge-shortcut and frontal detachment faults. Natural examples of this end-member have been described by Bergh et al. (1997) from the Tertiary Spitsbergen thrust belt. Here, the pre-rift section is represented by a mechanically strong pre-Upper Silurian basement. The syn-rift fill is formed by Upper Silurian–Devonian and Lower Carboniferous clastic sediments. The relatively strong post-rift section consists of Upper Carboniferous–Lower Permian carbonates with some evaporites, Triassic–Cretaceous siliciclastic sediments and Tertiary foreland basin strata. Various portions of the thrustbelt contain reactivated graben-bounding faults, footwall edge shortcut faults and detachment faults. Another example of an inversional structure involving predominantly strong lithologies and showing reactivated extensional, footwall edge-shortcut and detachment faults comes from the Northern Pyrenees, a Late Cretaceous–Early Miocene contractional orogen with inverted fills of Early Cretaceous extensional basins (Garcia-Senz et al., 2000). Here, the mechanically strong pre-, syn- and post-rift rift packages contain Jurassic carbonates, Lower Cretaceous dolostones and Albian carbonates (including part of the upper Cretaceous turbidites, which are syn-inversional), respectively.

The second end-member with strong syn-rift fill and weak post-rift sediments (Fig. 4b) shows modeled inversion structures characterized by a reactivation of the listric normal fault and an active footwall edge-shortcut fault. No reactivation of the frontal detachment fault occurs. Instead, a high strain zone developed in continuation of the footwall edge-shortcut fault indicating its potential future propagation through the post-rift sediments. A comparable natural example comes from the Pannonian basin system (Fig. 8a). It is represented by the two relatively simple anticlines; one above the reactivated listric normal fault and one above the footwall edge-shortcut fault. Here, the pre- and syn-rift sections are mechanically strong and overlain by weak post-rift sediments.

The third modeled end-member with syn- and post-rift sedimentary sections both mechanically weak (Fig. 4e) shows a reactivation of the pre-existing listric normal fault only. In spite of the prescription of footwall edge-shortcut and shallow frontal detachment faults, they were both not reactivated during inversion. Instead, a high strain zone developed in continuation of the reactivated pre-existing listric normal fault indicating its potential propagation through the post-rift sediments. A corresponding field example can be found in the Pannonian basin system. In this particular example of a small inverted basin (Fig. 8b) weak lithologies dominate and control the overall mechanically weak character of the syn- and post-rift basin fill. The interpreted seismic section in Fig. 8b does not indicate any footwall edge-shortcut and detachment faults and the syn-rift fill is more deformed than its counterpart in Fig. 8a. On a much smaller scale, an analogous highly deformed mechanically weak hanging wall can be observed in the Bristol Channel near Watchet (see Fig. 9g). Natural examples of inverted half-grabens with a similar style of deformation can be found in the Broad Fourteens Basin, North Sea, where the Lower Triassic–Lower Cretaceous syn-rift fill is

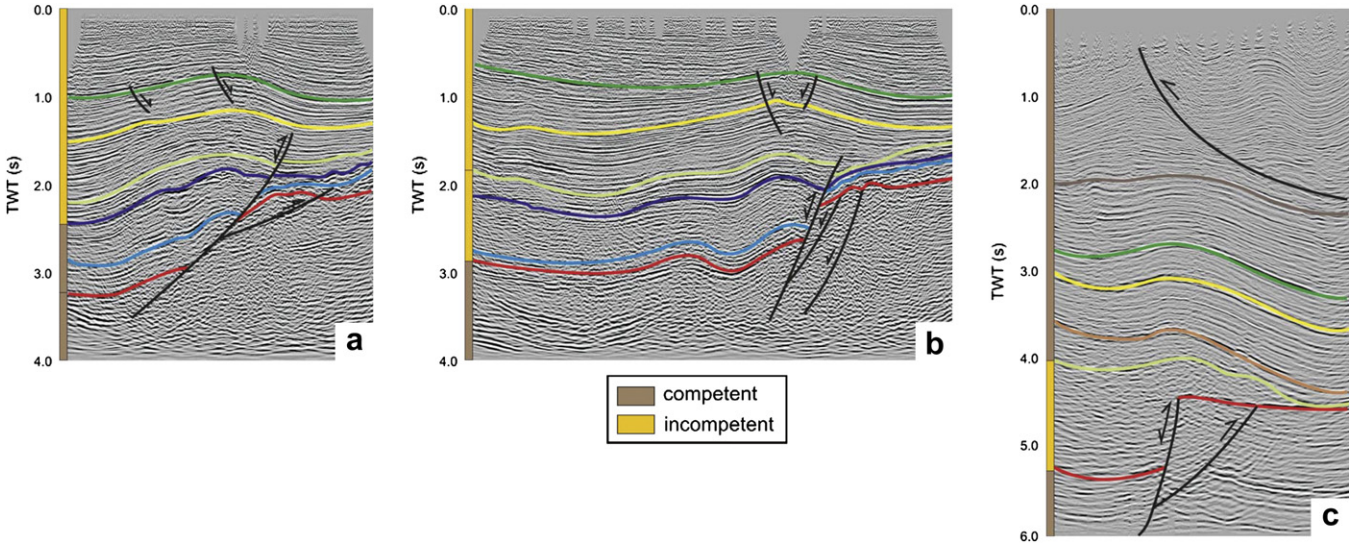

Fig. 8. Interpreted seismic sections through three small inverted extensional basins showing different styles of deformation depending on the mechanical properties of the pre-, syn- and post-rift section. These data come from the Pannonian basin area (a, b) and Georgia (c), however, the exact locations of the cross sections cannot be disclosed for confidentiality reasons. Vertical scale is in seconds two-way travel time (TWT). (a) Inversion has resulted in reactivation of the boundary fault as reverse fault and development of a footwall edge shortcut fault with reverse sense of displacement, respectively. In this example, mechanically strong lithologies in the pre- and syn-rift basin fill are overlain by a weak post-rift section (compare to Fig. 4b). (b) The style of deformation is different from case (a) if both the syn- and post-rift sections are composed of mechanically weak rocks. In this case, inversion leads to reactivation of the boundary fault as reverse fault, but no footwall edge shortcut fault has developed (compare to Fig. 4e). Note, that unlike neighbor case (a), this cross section cuts through the shale-dominant part of the syn-rift fill, which further lacks several sandstone beams due to erosion/non-deposition. (c) This seismic section is too shallow to reach the syn-rift and pre-rift sections. However, well data indicates that the imaged post-rift section can be divided into three rheologically distinct sediment packages, i.e. a mechanically weak lithology in between two strong rock layers (compare to Fig. 4f).

shale-dominated and the Upper Cretaceous post-rift fill is chalk-dominated. Inversion, which started during Turonian–Coniacian in different parts of the basin and ended during Maastrichtian, reactivated pre-existing normal faults, respectively propagated them a bit further, but did not develop any footwall edge-shortcut or detachment faults, as it can be seen from interpreted seismic sections (e.g., Badley et al., 1989). Yet another natural example has been reported from the Sunda Arc (Letouzey, 1990), where mechanically weak syn-rift and relatively weak post-rift sections are formed by the shale-dominant Eocene–lower Oligocene Pematang formation and shale-dominant upper Oligocene–lower Miocene Sihapas group, respectively. In addition, Late Miocene–Pliocene inversion was coeval with hydrocarbon expulsion from the organic-rich Pematang formation, which further enhanced its mechanically weak character.

Finally, the fourth end-member characterized by weak syn-rift sediments and strong post-rift sediments (Fig. 4f) shows reactivation of the pre-existing listric normal fault, and active footwall edge-shortcut and frontal detachment faults. Natural examples for this scenario are rare, but an oil-producing inversion structure from the Caucasian Kura Valley in Georgia can serve as a geometric analog with analogous lithologies. Seismic acquisition in this case (Fig. 8c) was not done deep enough to image the syn-rift section. However, the imaged Oligocene–lower Miocene portion of the post-rift section occupies only the graben, which remained unfilled after the period of rifting. Therefore, this shale-dominant, organic rich section located only in the graben can form a rheologic analog for a mechanically weak syn-rift fill. The post-lower Miocene portion of the post-rift section with numerous sandstone and conglomerate layers spreads beyond the boundary faults of the underlying graben. Therefore, it can be used as an analog for the mechanically strong post-rift section. Unpublished data from the oil field indicate the Pliocene growth of the inversional anticline. The inversional structure is characterized by a reactivated pre-existing listric normal fault and a newly formed footwall edge-shortcut fault, which are similar to those from the model (compare Figs. 8c and 4f).

5.2. Inversion-related fracture patterns

In order to assess the predictive potential of the inversion models with respect to fracture types and orientations, modeling results need to be compared to outcrop data. To be comparable to the numerical simulations, field examples require normal faults with simple listric geometries, which were later reactivated by contraction. Similarly, outcrops should not contain highly anisotropic multilayers and inversion should not be too strong to avoid the development of numerous generations of overprinting fracture sets.

Several field examples fulfilling these requirements were found in the Bristol Channel, British Isles. At visited outcrops (Fig. 9a), numerous normal faults, which were not affected by inversion, indicate that inversion was not very strong in the study area (Fig. 9b and c). This conclusion is based on a comparison with areas such as the South Hewett fault region, North Sea, where relatively small amounts of positive inversion resulted in reactivation of only a few isolated faults (see McClay, 1995). The relatively small amount of inversion

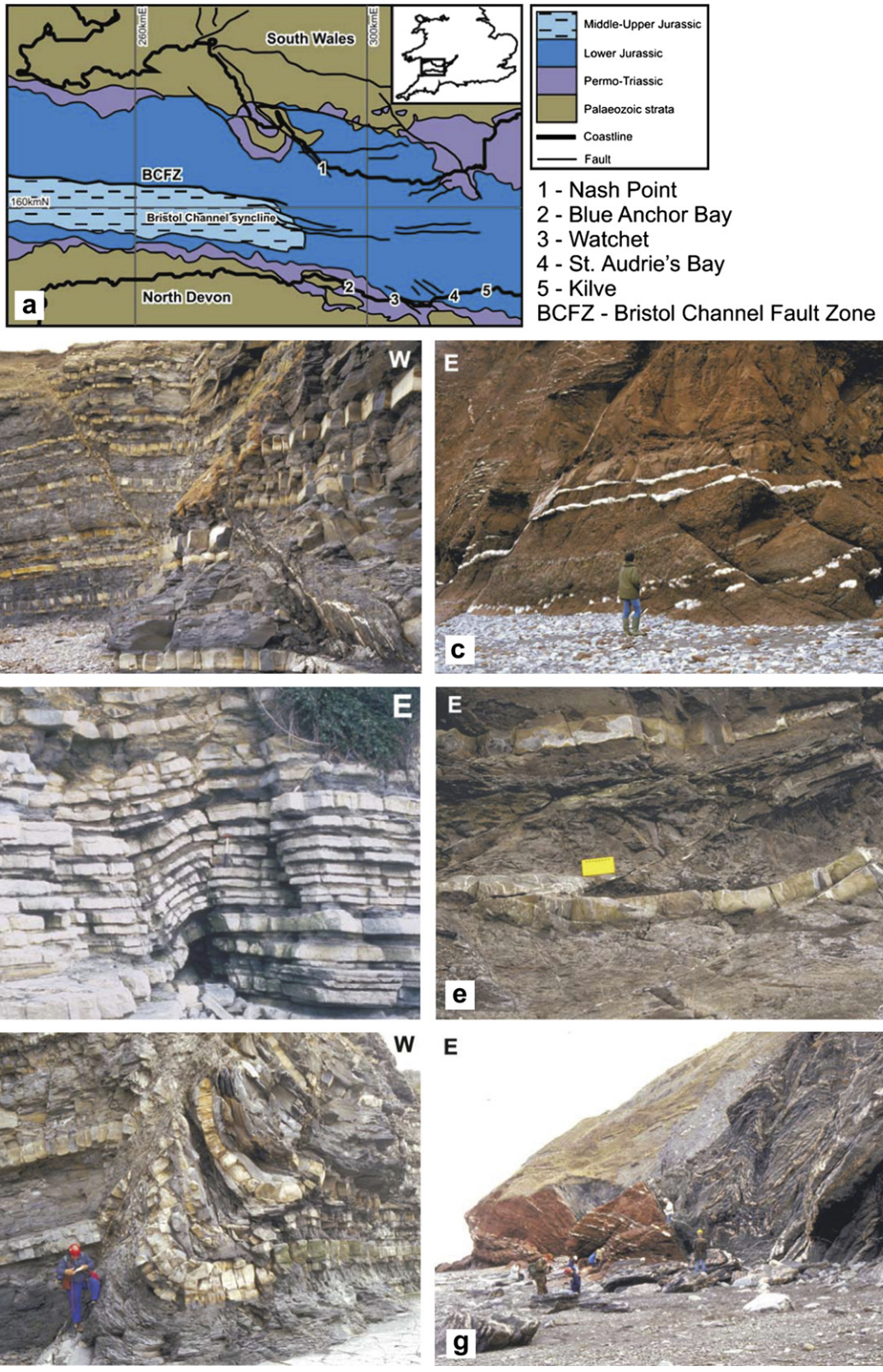
a
South Wales
North Devon
BCFZ
Bristol Channel syncline
160kmN
260kmE
300kmE
1
2
3
4
5
Middle-Upper Jurassic
Lower Jurassic
Permo-Triassic
Palaeozoic strata
Coastline
Fault
1 - Nash Point
2 - Blue Anchor Bay
3 - Watchet
4 - St. Audrie's Bay
5 - Kilve
BCFZ - Bristol Channel Fault Zone
b
c
d
e
f
g
E
W

observed in the various outcrops would match with the model documented in Fig. 7a, which shows the fracture patterns associated with the early stages of inversion for relatively strong syn-rift sediments. At the outcrop scale, a similar scenario is shown in Fig. 9d. In accordance with the model predictions in Fig. 7a, the outcrop contains a set of tensile fractures, which developed in the frontal of the two anticlines forming the inversional structure above the reactivated pre-existing listric normal fault. Like in the model, the fractures are steeply dipping and parallel to the fold axis. The outcrop also contains a region unaffected by fracturing. It occurs in portion of the main anticlinal core, which is located near the reactivated normal fault. Fault rock composition and fault zone cementation in the various outcrops suggest a friction coefficient of 0.4 according to guidelines of Hardcastle (1989) which is the same used for the numerical models.

Outcrops in hanging walls, which are located at larger distance from the reactivated listric normal fault, contain numerous shear fractures. Like in the models shown in Fig. 7a–c, these fracture sets are represented by a conjugate system of small-scale thrust faults, which are bisected by a sub-horizontal to slightly inclined σ_1 stress direction. The orientation of the shear fractures varies in relation to the stress perturbations in various parts of the hanging wall during the time of syn-inversional fracturing (Fig. 9e).

Footwall outcrops indicate that the pre-existing listric normal fault had high enough friction during the time of inversion to allow for a stress transfer, which succeeded in developing stress conditions large enough for shear fracturing in the footwall (Fig. 9f). Back-thrusts, with respect to the reactivated listric normal fault, dominate over the thrusts in this fracture set. They are dipping away from the reactivated normal fault at angles close to 50–60 °, which indicate that a controlling σ_1 stress was dipping away from the reactivated normal fault. This is in accordance with stress perturbations computed for models shown in Fig. 7a–c. Their footwall areas affected by shear fracturing are also relatively close to the reactivated main fault.

6. Conclusions

The results of the numerical simulations provide end-member scenarios for the style of deformation and templates for the prediction of fracture patterns in inversion structures. Stress and strain as well as the related fracture types and orientations in inverted half-grabens critically depend on the rheology of the affected rock section and stress transfer through the hanging wall.

Several conclusions can be drawn from the modeling results and the comparison with natural examples:

- For any given syn-rift lithology, a stronger post-rift section favors the development of a footwall edge-shortcut fault and a shallow frontal detachment fault, in addition to the reactivation of the pre-existing listric normal fault.
- Weaker syn-rift fills favor the reactivation of pre-existing listric normal faults instead of the footwall edge-shortcut fault, although this can be partly counteracted by stronger post-rift sediments. In case of a high mechanical contrast between syn- and post-rift sections, contraction may trigger development of independent imbricate thrusting in various structural levels.
- Stronger syn-rift rocks combined with weaker post-rift sections result in reactivation of the pre-existing listric normal fault and mobilization of the footwall edge-shortcut fault. Significantly thick weaker post-rift section can eventually cause the activity of the shallow frontal detachment fault.
- Stresses during inversion vary depending on whether the growing structure is being eroded or deposited on as it grows. Pressure-dependence of the yield strength makes a basin that is subject to deposition, mechanically stronger, while erosion weakens it. Thus, deposition acts against inversion and further growth, while erosion facilitates inversion.
- Principal stresses in the growing inversional structure are not only horizontal and vertical. Internal shear and

Fig. 9. Field examples from the Bristol Channel area showing outcrop-scale deformation styles related to inversion. (a) Simplified geological map of the inner Bristol Channel with location of studied outcrops. Inset shows the location of the study area in the southern British Isles. (b) Uninverted SSW-dipping normal fault in the calcareous mudstone and bioclastic calcilutite multilayer of the Lower Jurassic sedimentary section between Kilve and St Audrie's Bay. The multilayer is slightly mudstone-dominated. Footwall is relatively undeformed, hanging wall contains a gentle synform caused by the normal drag. Lower right corner of the photograph shows a fault core represented by calcite slickenside with dip-slip striations. (c) Two meso-scale SSW-dipping listric normal faults developed in the red Upper Triassic Mercia Mudstones, containing white bedding-parallel gypsum veins. Fault growth character is indicated by the total displacement progressively increasing with stratigraphic age. This can be illustrated by the offset of two couples of gypsum veins. The upper vein of the upper couple is barely offset by the left fault; the vein below has a couple tens of centimeters large offset. A vein couple at the bottom of the outcrop indicates almost one meter of offset. (d) Inverted NNE-dipping normal fault near Nash Point developed in interbedded calcareous mudstone and bioclastic calcilutite multilayer of the Lower Jurassic sedimentary section. Unlike the field examples in Fig. 9b, e and f, this multilayer is calcilutite-dominated. Crest of the anticline above the tip of the inverted fault is deformed by a set of tensile fractures parallel to the fold axis; the hanging wall below this deformation zone does not contain any fractures. (e) Hanging wall of the NNE-dipping inverted normal fault between Kilve and St Audrie's Bay developed in interbedded calcareous mudstone and bioclastic calcilutite rocks of the Lower Jurassic sedimentary section. The multilayer is slightly mudstone-dominated. Both mudstone and calcilutite layers are deformed by a meso-scale system of conjugate thrust faults. Their kinematics is documented by several tens of centimeters displacement of the calcilutite layers and striations on calcite slickensides. (f) The inverted NNE-dipping Blue Ben Fault between Kilve and St Audrie's Bay developed in interbedded calcareous mudstone and bioclastic calcilutite multilayer of the Lower Jurassic sedimentary section. The multilayer is slightly mudstone-dominated. Note relatively undeformed hanging wall and highly deformed footwall. Deformation in the footwall consists of synform developed by reverse drag. It is cut by a system of NNE-dipping meso-scale reverse faults, affecting both mudstone and calcilutite layers. The thick calcilutite layer in the crestal portion of the synform contains a set of tensile fractures caused by release of flexural stresses. They are parallel to the fold axis. (g) Highly deformed gray Upper Triassic Blue Anchor Beds at Warren Bay, between Watchet and Blue Anchor Bay, in the hanging wall of the inverted normal fault. The deformation was caused by buttressing against the SSW-dipping normal fault. The footwall is formed by relatively undeformed red Upper Triassic Mercia Mudstone, containing white bedding-parallel gypsum veins.

proximity to faults result in local stress perturbations, which in turn cause variable fracture orientation throughout the inverted half-graben.

Comparison of natural and modeled fracture sets indicates that the described models are capable of indicating the main fracture trends for multilayers, which do not have relatively high degree of anisotropy. Future modeling work focusing on multilayers with high degree of anisotropy will require the exact definition of layers of interest to be able to simulate the different deformation mechanisms of individual layers. In addition, deformation and fracturing achieved during earlier inversion development stages will have to be carried on and prescribed to the subsequent development stage.

Acknowledgments

J.-D. van Wees and A. Pfiffner are thanked for their helpful comments on an earlier version of the manuscript. This study was made within the project "Systematics of hydrocarbon exploration and production in thrustbelts" sponsored by Elf, Enterprise, Occidental, Repsol YPF and Texaco.

References

Al-Musallam, Z., Elders, C.F., McClay, K.R., 2002. 4D analysis of inversion kinematics, southern North Sea. AAPG annual convention with SEPM, 10–13 March, 2002, Houston, TX, USA. Annual Meeting Expanded Abstracts, American Association of Petroleum Geologists, pp. 3.

Badley, M.E., Price, J.D., Backshall, L.C., 1989. Inversion, reactivated faults and related structures: seismic examples from the southern North Sea. In: Cooper, M.A., Williams, G.D. (Eds.), Inversion Tectonics. Special Publications, vol. 44. Geology Society, London, pp. 201–219.

Bally, A.W., 1983. Seismic expression of structural styles: a picture and work atlas. American Association of Petroleum Geologists Studies in Geology 15 (three separate atlases).

Beekman, F., Badsi, M., Van Wees, J.-D., 2000. Faulting, fracturing and in-situ stress prediction in hydrocarbon reservoirs: a finite element approach. Tectonophysics 320, 311–329.

Bergh, S.G., Braathen, A., Andresen, A., 1997. Interaction of basement-involved and thin-skinned tectonism in the Tertiary fold-thrust belt of central Spitsbergen, Svalbard. American Association of Petroleum Geologists Bulletin 81, 637–661.

Blay, P., Cosgrove, J.W., Summers, J.M., 1977. An experimental investigation of the development of structures in multilayers under the influence of gravity. Journal of the Geological Society, London, vol. 133, 329–342.

Bott, M.H.P., Dean, D.S., 1973. Stress diffusion from plate boundaries. Nature 243, 339–341.

Brun, J.-P., Nalpas, T., 1996. Graben inversion in nature and experiments. Tectonics 15, 677–687.

Buchanan, P.G., McClay, K.R., 1991. Sandbox experiments of inverted listric and planar fault systems. Tectonophysics 188, 97–115.

Buiter, S.J.H., Pfiffner, O.A., 2003. Numerical models of the inversion of half-graben basins. Tectonics 22 (5), 1057, doi:10.1029/2002TC001417.

Clark Jr., S.P., 1966. Handbook of physical constants. GSA Memoir. New York, vol. 97, 1–587.

Cloetingh, S.A.P.L., Zoetemeijer, R., van Wees, J.D., 1995. Tectonics I. Tectonics and basin formation in convergent settings: thermo-mechanical evolution of the lithosphere and basin evolution in compressive tectonic regimes. Short Course. Vrije University, Amsterdam.

Cooper, M.A., Williams, G.D., de Graciansky, P.C., Murphy, R.W., Needham, T., De Paor, D.G., Stoneley, R., Todd, S.P., Turner, J.P., Ziegler, P.A., 1989. Inversion tectonics: a discussion. In: Cooper, M.A., Williams, G.D. (Eds.), Inversion tectonics meeting. Special Publications, vol. 44. Geological Society, pp. 335–347.

Couples, G.D., Lewis, H., 1998. Lateral variations of strain in experimental forced folds. Tectonophysics 295, 79–91.

Couples, G.D., Stearns, D.L., Handin, J.W., 1994. Kinematics of experimental forced folds and their relevance to cross-section balancing. Tectonophysics 233, 193–213.

Coward, M.P., 1994. Inversion tectonics. In: Hancock, P.L. (Ed.), Continental deformation. Pergamon Press, Tarrytown, NY, pp. 289–304.

Coward, M.P., Enfield, M.A., Fischer, M.W., 1989. Devonian basins of northern Scotland: extension and inversion related to Late Caledonian–Variscan tectonics. In: Cooper, M.A., Williams, G.D. (Eds.), Inversion tectonics meeting. Special Publication, vol. 44. Geological Society, London, pp. 275–308.

Davis, P.N., 1983. Gippsland Basin, southeastern Australia. In: Bally, A.W. (Ed.), Seismic Expression of Structural Styles: A Picture and Work Atlas. American Association of Petroleum Geologists Studies in Geology, series 15, vol. 3, pp. 3.3-19–3.3-24.

De Jager, J., Doyle, M.A., Grantham, P.J., Mabillard, J.E., 1993. Hydrocarbon habitat of the West Netherlands Basin. In: Rondeel, H.E., Batjes, D.A.J., Nieuwenhuijs, W.H. (Eds.), Geology of gas and oil under the Netherlands. Royal Geological and Mining Society of the Netherlands/Kluwer Academic Publishers, Dordrecht, pp. 191–209.

Eisenstadt, G., Withjack, M.O., 1995. Estimating inversion: results from clay models. In: Buchanan, J.G., Buchanan, P.G. (Eds.), Basin inversion. Special Publications, vol. 88. Geological Society, London, pp. 119–136.

Ferguson, A., McClay, K.R., 2000. Detached inversion: a new structural style applied to the Mahakam fold belt, Kutai Basin, East Kalimantan, Indonesia. American Association of Petroleum Geologists Bulletin 84, 1425.

Fraser, A.J., Nash, D.F., Steele, R.P., Ebdon, C.C., 1990. A regional assessment of the intra-Carboniferous play of Northern England. In: Brooks, J. (Ed.), Classic petroleum provinces. Special Publications, vol. 50. Geological Society, London, pp. 417–440.

Friedman, M., Handin, J., Logan, J.M., Min, K.D., Stearns, D.W., 1976a. Experimental folding of rocks under confining pressure, Part III: Faulted drape folds in multilithologic layered specimens. Geological Society of America Bulletin, vol. 87, 1049–1066.

Friedman, M., Hugman, R.H.H., Handin, J., 1980. Experimental folding of rocks under confining pressure, Part VIII: Forced folding of unconsolidated sand and lubricated layers of limestone and sandstone. Geological Society of America Bulletin, vol. 91, 307–312.

Friedman, M., Teufel, L.W., Morse, J.D., 1976b. Strain and stress analyses from calcite twin lamellae in experimental buckles and faulted drape folds. Philosophical Transactions of the Royal Society of London 4283, 87–107.

Garcia-Senz, J., Munoz, J.A., McClay, K.R., 2000. Inversion of Early Cretaceous extensional basins in the central Spanish Pyrenees. AAPG international conference, abstracts, 15-18 October, 2000, Bali, Indonesia. AAPG Bulletin 84 (9), 1428–1429.

Geiser, P., 1974. Cleavage in some sedimentary rocks of the central Valley and Ridge province. Maryland. Geological Society of America Bulletin, vol. 85, 1399–1412.

Gibbs, A.D., 1987. Linked tectonics of the northern North Sea basins. In: Beaumont, C., Tankard, A.J. (Eds.), Sedimentary basins and basin-forming mechanisms. Atlantic Geoscience Society Special Publication, 5, pp. 163–171.

Hardcastle, K.C., 1989. Possible paleostress tensor configurations derived from fault – slip data in eastern Vermont and western New Hampshire. Tectonics 8, 265–284.

Hayward, A.B., Graham, R.H., 1989. Some geometrical characteristics of inversion. Geological Society. Special Publications, vol. 44, 17–39.

Horváth, F., Cloetingh, S.A.P.L., 1996. Stress-induced late-stage subsidence anomalies in the Pannonian basin. Tectonophysics 266, 287–300.

Jaeger, J.C., Cook, N.G.W., 1979. Fundamentals of rock mechanics. Chapman & Hall, London. 1-593.

Johnson, K.M., Johnson, A.M., 2002a. Mechanical models of trishear-like folds. Journal of Structural Geology 24, 277–287.

Johnson, K.M., Johnson, A.M., 2002b. Mechanical analysis of the geometry of forced-folds. Journal of Structural Geology 24, 401–410.

Koopman, A., Speksnijder, A., Horsfield, W.T., 1987. Sandbox model studies of inversion tectonics. Tectonophysics 137, 379–388.

Koyi, H., 1995. Mode of internal deformation in sand wedges. Journal of Structural Geology 17, 293–300.

Koyi, H., 1997. Analogue modeling: from a qualitative to a quantitative technique, a historical outline. Journal of Petroleum Geology 20, 223–238.

Kuhle, N.J., Chester, J.S., Chester, F.M., 2001. Kinematics of inversion of normal-faulted strata as a function of burial depth and rock ductility. Geological Society of America, 2001 annual meeting, Boston, MA (Abstracts with Programs). Geological Society of America, vol. 33 (6), 150 pp.

Lama, R.D., Vutukuri, V.S., 1978. Handbook on mechanical properties of rocks, Transtech Publications. Bay Village, vol. 2, 1–481.

Letouzey, J., 1990. Petroleum and tectonics in mobile belts. Proceedings of the IFP exploration and production research conference. Technip, Paris.

Letouzey, J., Colletta, B., Benard, F., Sassi, W., Bale, P., 1990. Fault reactivation and structural inversion physical models analyzed with X-ray scanner and seismic examples. In: Anonymous (Ed.), AAPG Annual Convention with DPA/EMD Divisions and SEPM, an Associated Society: Technical Program with Abstracts. American Association of Petroleum Geologists Bulletin, 74, pp. 703–704.

Logan, J.M., Friedman, M., Stearns, M.T., 1978. Experimental folding of rocks under confining pressure, Part VI: Further studies of faulted drape folds. In: Mathews, V. (Ed.), Laramide Folding Associated with Basement Block Faulting in the Western United States, vol. 151. Geological Society of America Memoir, pp. 79–99.

Lowell, J.D., 1995. Mechanics of basin inversion from worldwide examples. In: Buchanan, J.G., Buchanan, P.G. (Eds.), Basin Inversion. Special Publications, vol. 88. Geological Society, London, pp. 39–57.

Mandl, G., 1988. Mechanics of Tectonic Faulting. Models and Basic Concepts. Elsevier, Amsterdam. 407.

McClay, K.R., 1995. The geometries and kinematics of inverted fault systems: a review of analogue model studies. In: Buchanan, J.G., Buchanan, P.G. (Eds.), Basin Inversion. Special Publication, vol. 88. Geological Society, London, pp. 97–118.

Mitra, S., 1987. Regional variations in deformation mechanisms and structural styles in the central Appalachian orogenic belt. Geological Society of America Bulletin 98, 569–590.

Nalpas, T., Douaran, S., Le Brun, J.P., Unternehr, P., Richert, J.P., 1995. Inversion of the Broad Fourteens Basin (offshore Netherlands): a small-scale model investigation. Sedimentary Geology 95, 237–250.

Nemčok, M., Krzywiec, P., Wojtaszek, M., Ludhová, L., Klecker, R.A., Sercombe, W.J., Coward, M.P., 2006. Tertiary development of the Polish and Eastern Slovakian parts of the Carpathian accretionary wedge: insights from balanced cross sections. Geologica Carpathica 57 (5), 355–370.

Nemčok, M., Schamel, S., Gayer, R.A., 2005. Thrustbelts: Structural Architecture, Thermal Regimes and Petroleum Systems. Cambridge University Press, Cambridge, 541 pp.

Panien, M., Schreurs, G., Pfiffner, A., 2005. Sandbox experiments on basin inversion: testing the influence of basin orientation and basin fill. Journal of Structural Geology 27, 433–445.

Patton, T.L., Logan, J.M., Friedman, M., 1998. Experimentally generated normal faults in single- and multilayer limestone beams at confining pressure. Tectonophysics 295, 53–77.

Roberts, D.G., 1989. Basin inversion in and around the British Isles. In: Special Publication, vol. 44. Geological Society, London. 3–16.

Sassi, W., Faure, J.L., 1996. Role of faults and layer interfaces on the spatial variation of stress regimes in basins; inferences from numerical modelling. Tectonophysics 266, 101–119.

Schedl, A., Wiltschko, D.V., 1987. Possible effects of pre-existing basement topography on thrust fault ramping. Journal of Structural Geology 9, 1029–1037.

Scholz, C.H., 1968. Microfracturing and the inelastic deformation of rock in compression. Journal of Geophysical Research 73, 1417–1432.

Selley, R.C., Stoneley, R., 1987. Petroleum habitat in south Dorset. In: Brooks, J., Glennie, K.W. (Eds.), Petroleum Geology of Northwest Europe. Graham and Trotman, London, pp. 623–632.

Sibson, R.H., 1996. Structural permeability of fluid-driven fault-fracture meshes. Journal of Structural Geology 18, 1031–1042.

Stearns, D.W., Weinberg, D.M., 1975. A comparison of experimentally created and naturally formed drape folds. Wyoming Geological Association Guidebook 27, 159–166.

Townend, J., Zoback, M.D., 2000. How faulting keeps the crust strong. Geology 28, 399–402.

Turcotte, D.L., Schubert, G., 2002. Geodynamics, second ed. Cambridge University Press, Cambridge, 456 pp.

Uliana, M.A., Arteaga, M.E., Legarreta, L., Cerdan, J.J., Perono, G.O., 1995. Inversion structures and hydrocarbon occurrence in Argentina. In: Buchanan, J.G., Buchanan, P.G. (Eds.), Basin Inversion. Special Publications, vol. 88. Geological Society, London, pp. 211–233.

Ulmishek, G.F., Bogino, V.A., Keller, M.B., Poznyakevich, Z.L., 1994. Structure, stratigraphy, and petroleum geology of the Pripyat and Dnieper–Donets basins, Byelarus and Ukraine. In: Landon, S.M. (Ed.), Interior Rift Basins. American Association of Petroleum Geologists Memoir, 59, pp. 125–156.

van Wees, J.D., Orlic, B., van Eijs, R., Zijl, W., Jongerius, P., Schreppers, G.J., Hendriks, M., Cornu, T., 2003. Integrated 3D geomechanical modelling for deep subsurface deformation: a case study of tectonic and human-induced deformation in the eastern Netherlands. In: Nieuwland, D.A. (Ed.), New Insights into Structural Interpretation and Modelling. Special Publications, vol. 212. Geological Society, London, pp. 313–328.

Weinberg, D.M., 1979. Experimental folding of rocks under confining pressure, Part VII: Partially scaled models of drape folds. Tectonophysics 54, 1–24.

Wiltschko, D.V., Eastman, D., 1983. Role of basement warps and faults in localizing thrust fault ramp. In: Hatcher, R.D., Williams, H., Zietz, I. (Eds.), Contributions to the Tectonics and Geophysics of Mountain Chains. Geological Society of America Memoirs, 158, pp. 177–190.

Wojtal, S., Mitra, G., 1986. Strain hardening and strain softening in fault zones from foreland thrusts. Geological Society of America Bulletin 97, 674–687.

Yamada, Y., McClay, K.R., 2003. Application of geometric models to inverted listric fault systems in sandbox experiments, Paper 1: 2D hanging wall deformation and section restoration. Journal of Structural Geology 25 (9), 1551–1560.